NJC

ROYAL SOCIETY OF CHEMISTRY

PAPER

View Article Online
View Journal | View Issue

Cite this: *New J. Chem.*, 2025, **49**, 8454

Innovative CuBTC/g-C_3N_4 materials for tetracycline mitigation: adsorption, photocatalysis, and mechanistic perspectives†

Palkaran Sethi,[a] Soumen Basu *[a] and Sanghamitra Barman *[b]

The widespread accumulation of antibiotic pollutants in water sources calls for advanced and efficient remediation strategies to curb environmental contamination. In this study, a CuBTC (copper benzene-1,3,5-tricarboxylate) with g-C_3N_4 heterojunction photocatalyst was synthesized *via* a hydrothermal approach in varying ratios (1 : 1, 1 : 3, and 3 : 1) and comprehensively characterized using XRD, FESEM, EDS, HRTEM, EIS, UV-DRS, PL, TGA, FTIR, XPS, and BET measurements, confirming the composite's crystallinity, morphology, elemental composition, charge transport properties, optical behavior, stability, and porosity. Among the tested compositions, the 3 : 1 CuBTC/g-C_3N_4 composite exhibited the highest efficiency, achieving an impressive 97.4% degradation of 25 ppm tetracycline (TC) within just 60 minutes under UV illumination, with a remarkable rate constant of 0.02098 min^{-1}. Stability assessments confirmed its excellent reusability over six consecutive cycles, with only a slight decline in performance to 82.7%. The adsorption behaviour of the composite was analyzed using six isotherm models—Langmuir, Freundlich, Halsey, Harkins–Jura, Temkin, and Dubinin–Radushkevich—along with five kinetic models, including pseudo-first-order, pseudo-second-order, intraparticle diffusion, Elovich, and liquid film models. Adsorption followed the Langmuir isotherm (R^2 = 0.992) and pseudo-second-order kinetics (R^2 = 0.968), while photocatalytic degradation aligned with pseudo-second-order kinetics (R^2 = 0.993). Mechanistic studies identified superoxide radicals as the primary reactive species, supported by hydroxyl radicals, electrons, and holes in the degradation pathway. Mineralization studies revealed significant reductions in TOC (67.8%) and COD (68.6%), while LC-MS analysis provided a comprehensive degradation pathway, illustrating the breakdown of TC into intermediates through ring-opening and oxidative transformations. Thermodynamic assessments indicated that the degradation process was exothermic and spontaneous. ΔG, ΔH and ΔS values were found to be 92.7 J mol^{-1}, −63.84 kJ mol^{-1}, and −0.214 kJ mol^{-1} K^{-1} respectively.

Received 10th February 2025,
Accepted 8th April 2025

DOI: 10.1039/d5nj00556f

rsc.li/njc

1. Introduction

For over half a century, antibiotics have served as a vital shield, protecting humans and animals from diverse pathogens. In recent times, however, their production and use have surged dramatically. Global antibiotic consumption was expected to soar to 128 billion defined daily doses by 2023, marking a staggering increase of over 200% since 2015.[1] The persistence of antibiotics in water sources has become a global concern due to their detrimental effects on the environment and the potential risks they pose to aquatic life. Consequently, they are now classified as emerging pollutants.[2–4] Key contributors to their presence in aquatic environments include pharmaceutical industries, municipal wastewater, hospital effluents, and sewage treatment plants.[5,6] Tetracycline a broad-spectrum antibiotic is extensively used in human and veterinary medicine, including salmon farming. Their overuse can cause serious health issues like nephropathy, central nervous system disturbances, and increased antibiotic resistance.[7] Residual antibiotics harm ecosystems and contribute to the emergence of bacterial strains with multi-drug resistance.[8] Thus, practical technological solutions are necessary for their elimination. Various approaches, such as physical adsorption,[9,10] chemical oxidation,[11] and biological treatments,[12] have been explored for removing tetracyclines (TCs). While each offers certain benefits, they often come with drawbacks, including complex procedures and risks of secondary pollution, limiting their

[a] *Department of Chemistry and Biochemistry, Thapar Institute of Engineering and Technology, Patiala-147004, Punjab, India. E-mail: soumen.basu@thapar.edu*
[b] *Department of Chemical Engineering, Thapar Institute of Engineering and Technology, Patiala-147004, Punjab, India. E-mail: sbarman@thapar.edu*

† Electronic supplementary information (ESI) available. See DOI: https://doi.org/10.1039/d5nj00556f

practical applications.[1,13] In contrast, photocatalysis presents advantages like simplicity, low energy consumption, high efficiency, and minimal secondary pollution.[14,15] However, photocatalysis can be hindered by rapid recombination of photogenerated carriers and limited interaction with low-concentration antibiotics, reducing its effectiveness. To address these limitations, a promising strategy combines adsorption and photocatalysis.[16–19] This approach enhances degradation by first rapidly capturing antibiotics through adsorption, followed by photocatalytic breakdown of the adsorbed pollutants and regeneration of the adsorbent.[15] Various materials, such as mineral adsorbents, resins, activated carbons, silicon materials, polymers, metal oxides, charcoal, coordination polymers, and metal–organic frameworks, have been employed for antibiotic adsorption due to their high surface area and functional properties, which play a key role in enhancing adsorption efficiency.[20] Coordination polymers (CPs) are highly crystalline and porous materials formed by transition metal ions and organic ligands.[21] With adjustable pore sizes, vast surface areas, and diverse structures, they excel in adsorption, separation, and catalysis. Their unique combination of metal clusters and organic linkers allows for efficient light absorption and electron transfer, positioning them as exciting contenders in photocatalysis.[8,22–26] CPs gain enhanced properties when combined with active materials. CP-carbon nanostructure composites have recently emerged as promising solutions for sustainable environmental applications. To enhance the photocatalytic activity of CPs, we integrate it with g-C_3N_4, transforming the composite into an efficient photocatalyst and combining the adsorption properties of CPs with the photocatalytic capabilities of g-C_3N_4. Graphite phase nitrogenized carbon (g-C_3N_4) is a non-metal semiconductor distinguished by its remarkable chemical stability, cost-effectiveness, and availability. Due to its remarkable photocatalytic efficiency, it is gaining heightened attention in the field of photocatalysis.[27–29] Recently, research on CP/g-C_3N_4 composites has expanded significantly, primarily concentrating on applications such as photocatalysis, fuel cells, and the oxygen reduction reaction, among others. For instance, a Ce-based CP/g-C_3N_4 composite demonstrated superior dye removal efficiency compared to Ce-based CP or g-C_3N_4 alone for the degradation of methylene blue when exposed to UV-visible light.[30] Cu-BTC, a well-known CP, has been widely explored for adsorption applications due to its high porosity and surface functionality. However, its direct application in antibiotic degradation has been limited due to its poor photo-reactivity as Cu-BTC itself does not effectively absorb any light.[31] The incorporation of g-C_3N_4 enhances the composite's photocatalytic performance by facilitating UV light absorption. Compared to other reported composites, such as TiO_2-based materials, Cu-BTC/g-C_3N_4 demonstrates superior adsorption capacity and photoreactivity, making it a promising candidate for antibiotic degradation offering a more effective and stable solution for environmental remediations.[7] Also, a Bi-based CP/g-C_3N_4 composite demonstrated exceptional photocatalytic efficiency for both pollutant degradation (rhodamine B) and nitrogen fixation, offering a promising approach to converting wastewater into nutrient-rich irrigation water, addressing both environmental and agricultural sustainability.[32] In another study, a range of MIL-88A composites doped with Ag/AgCl and supported on g-C_3N_4 were developed for the photocatalytic degradation of the herbicide Diuron.[33] Another composite, $AgFeO_2$/G@$Cu_2(BTC)_3$, exhibited superior photocatalytic efficiency under sunlight, achieving high removal rates for antibiotic pollutants and 87.1% COD reduction in real wastewater. The enhanced performance is due to efficient charge transfer *via* a Z-scheme mechanism facilitated by graphene.[34] Also, Fe-based CP doped sesame stalk biochar exhibited higher degradation rates of 92.5% and 86.7% for norfloxacin and tetracycline respectively.[35,36]

In comparison to CP/g-C_3N_4, MIL-88A/Ag/AgCl, and $AgFeO_2$/G@$Cu_2(BTC)_3$ composites, the Cu-BTC/g-C_3N_4 composite exhibits superior performance in antibiotic degradation because of its distinct structural and functional characteristics. Its adsorption capacity is improved by its much larger surface area, which surpasses 1000 $m^2\ g^{-1}$ and outperforms MIL-88A/Ag/AgCl and CP/g-C_3N_4. Achieving over 97% tetracycline degradation, the Z-scheme mechanism in Cu-BTC/g-C_3N_4 facilitates effective electron–hole separation, outperforming the plasmonic effect-based MIL-88A/Ag/AgCl and $AgFeO_2$/G@$Cu_2(BTC)_3$ composites. Furthermore, compared to Ag/AgCl composites that are prone to degradation, Cu-BTC/g-C_3N_4 shows better stability and reusability, maintaining its catalytic efficiency for more cycles with less metal leaching. Its innovative nature is further enhanced by its economical design and environmentally friendly synthesis, which position Cu-BTC/g-C_3N_4 as an excellent material for environmentally friendly wastewater treatment. Most of the composites fail to achieve optimal charge separation or consistent performance. To address this, we developed a CuBTC/g-C_3N_4 (CgC) composite in different ratios as CgC11 (1 : 1), CgC13 (1 : 3), and CgC31 (3 : 1). The catalysts were thoroughly analyzed employing techniques such as XRD, FESEM, EDS, HRTEM, EIS, UV-DRS, PL, TGA, FTIR, XPS, and BET. A sequence of experiments were meticulously crafted to elucidate the synergistic interaction between adsorption and photocatalysis of tetracycline. Thermodynamic parameters such as ΔH°, ΔG°, and ΔS° were diligently analyzed alongside adsorption isotherms, adsorption kinetics, and photocatalytic kinetic models. Additionally, potential mechanisms for the adsorption and photocatalytic degradation of tetracycline were proposed.

2. Experimental approach

2.1. Materials and methods

The materials were synthesized using high-purity reagents, including urea, cupric nitrate trihydrate, and trimesic acid all sourced from LOBA CHEMIE and GLR INNOVATIONS. Commercial tetracycline powder was obtained from Sigma Aldrich. Ultrapure double-distilled water was utilized for all solution preparations.

2.2. Synthesis

2.2.1. Synthesis of CuBTC. CuBTC (HKUST-1) was synthesized following the method by Williams and colleagues.[37] Copper nitrate (0.716 g, 3 mmol) and benzene tricarboxylic

acid (0.421 g, 2 mmol) were dissolved in a 12 mL ethanol–water mixture and stirred for 30 minutes at room temperature. The solution was subsequently transferred to a Teflon-lined autoclave and heated for 24 hours at 383 K. After crystallization, the autoclave was allowed to cool naturally. The resulting turquoise-blue crystals, designated as CBT, were sonicated for 5–10 minutes in a 50 : 50 EtOH–H_2O solution, filtered through Büchner filtration, and air-dried for 24 hours.[10,38,39]

2.2.2. Synthesis of g-C_3N_4 (graphitic carbon nitride). To prepare g-C_3N_4, 40 g of urea was first dissolved in 100 mL of water within a silica crucible and recrystallized by heating at 90 °C. The recrystallized urea was then scraped, wrapped in aluminum foil, and subjected to thermal treatment in a muffle furnace. The temperature was incrementally increased to 550 °C at a rate of 10 °C per minute and sustained for two hours. This process produced yellow-brown precipitates of g-C_3N_4, which were subsequently ground into a fine powder using a mortar and pestle, yielding the material referred to as GC.[40]

2.2.3. Synthesis of the CuBTC/g-C_3N_4 composite. A required amount of g-C_3N_4 solution in a 50 : 50 ethanol–water mixture was prepared by sonication for 1 hour in an ice bath. Then, benzene 1,3,5-tricarboxylic acid (0.421 g, 2 mmol) and Cu $(NO_3)_2{\cdot}3H_2O$ (0.716 g, 3 mmol) were dissolved in a 12 mL ethanol–water mixture. This solution was combined with the g-C_3N_4 suspension and sonicated vigorously for 15 minutes. The mixture was then added to a Teflon-lined autoclave and further heated at 383 K for 24 hours. After cooling to room temperature, the resulting hybrid nanocomposites were collected and sonicated in an ethanol–water solution for 5–10 minutes. These were then filtered and air-dried for 24 hours. Three distinct CgC composites—CgC11, CgC13, and CgC31—were synthesized by varying the Cu-BTC to g-C_3N_4 ratio at 1 : 1, 1 : 3, and 3 : 1, respectively (Scheme 1).

2.3. Characterization

Comprehensive characterization data, including analyses from FTIR, XRD, FESEM, BET, and other methods employed to verify the structural, surface, and morphological properties of the Cu-BTC/g-C_3N_4 composite, are available in the ESI.†

2.4. Adsorption and photocatalytic degradation experiments

The adsorption and photocatalytic experiment details are provided in the ESI.† All statistical analyses were performed using OriginPro 2018 64-bit (OriginLab, USA). Nonlinear regression was applied to fit the adsorption isotherm and kinetic models, as these equations do not follow a linear trend. Standard deviations were calculated from triplicate experiments, and 95% confidence intervals were determined to assess data reliability.

3. Results and discussion

3.1. Characterization of the CuBTC and g-C_3N_4 composites

CuBTC and g-C_3N_4 composites in 1 : 1, 1 : 3, and 3 : 1 ratios, termed CgC11, CgC13, and CgC31, were synthesized using a hydrothermal technique. The octahedral CuBTC was formed *in situ* between gC_3N_4 sheets.

3.1.1. XRD analysis. The XRD patterns of CB, GC, and their composites are shown in Fig. 1(a) which effectively confirm the purity and crystalline structure of the synthesized composites. For CB, the peaks at 6.66°, 9.5°, 11.64°, 13.42°, 17.5°, 19.08°, 20.24°, 26°, 29.34°, 36.7°, 39.38° and 47.14° were detected, corresponding to the (200), (220), (222), (440), (422), (511), (440), (660), (730), (751), (773), (828), and (751) planes, confirming the successful synthesis of the CUBTC structure.[41]

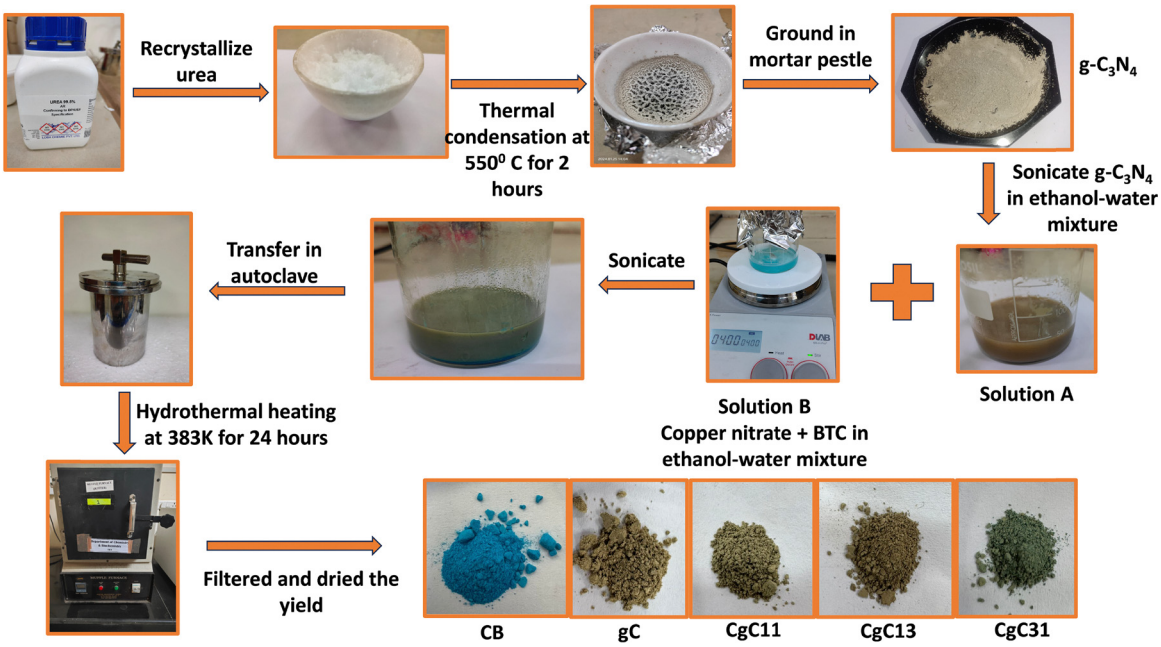

Scheme 1 Schematic illustration of the synthesis process for CgC composites.

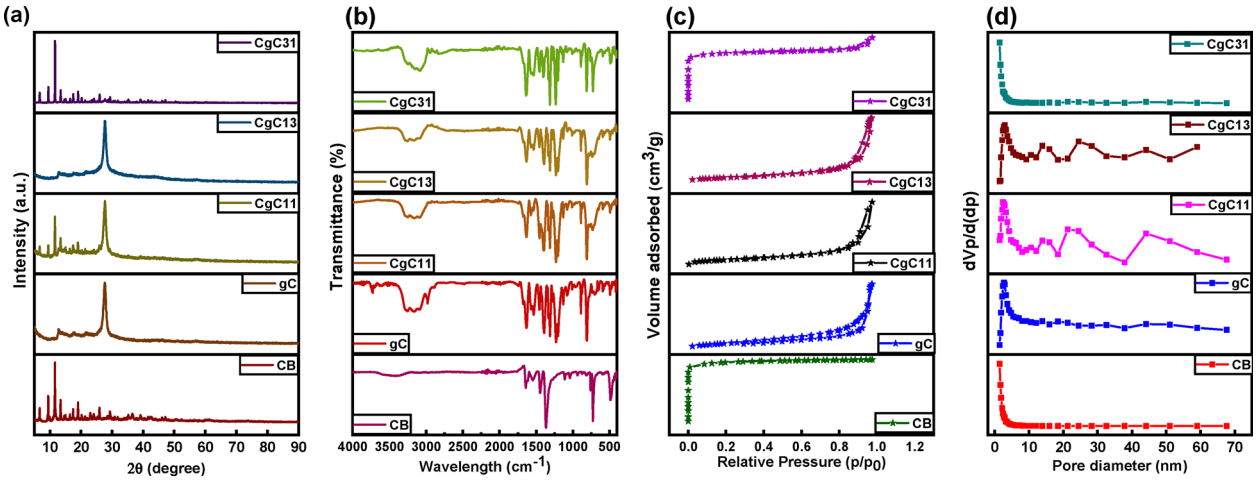

Fig. 1 (a) XRD spectra, (b) FT-IR spectra, (c) BET surface area isotherms and (d) BJH plots of CB, g-C_3N_4, CgC11, CgC13, and CgC31.

A peak at 27.46°, corresponding to the (002) crystal plane, was observed for GC, which is its characteristic peak.[42] The XRD pattern of all the hybrid composites aligned well with those of CB and GC, indicating the formation of GC nanosheets and the CB structure in the nanocomposite. Compared to pure CB and GC, the XRD patterns of the composites showed slight shifting in the peaks, suggesting possible interactions between them. The relative crystallinity of CB remained intact, which may influence adsorption performance. These findings align with previous studies on heterojunctions,[36] where crystallinity plays a key role in adsorption efficiency and material stability.

3.1.2. FT-IR measurement. The FTIR spectra of CB, GC, and their composites are presented in Fig. 1(b) In GC, a broad peak between 3000 and 3300 cm^{-1} was observed, corresponding to the N—H stretching vibration, while bands in the 1200–1650 cm^{-1} range, with specific peaks at 1223, 1309, 1396, 1458, 1535, and 1637 cm^{-1}, were attributed to C—N and C≡N within heterocycles. The triazine breathing mode was noted at 809 cm^{-1}.[43] For CB, distinctive peaks were observed at approximately 3300 cm^{-1} (O–H/–OH), 1644 and 1547 cm^{-1} (asymmetric $-CO_2-$), 1442 and 1365 cm^{-1} (BTC carboxylate), and 1111 cm^{-1} (C–O–Cu), with benzene ring C–H bending vibrations at 760 and 728 cm^{-1}.[44] The observed shifts in key functional group vibrations, such as the stretching modes of Cu–O and C–N bonds, provided evidence of strong interactions between CB and gC in the composites. Specifically, the shift in the Cu–O stretching band indicated coordination changes due to the integration of g-C_3N_4, while the variations in the C–N stretching region suggested electronic interactions between the two components. The nanocomposites exhibited absorption peaks associated with these functional groups, with minor shifts in wavenumbers, indicating the successful formation of the hybrid nanocomposites.[45]

3.1.3. BET surface area analysis. The BET surface area, pore size distribution, and total pore volume of CB, gC, and their composites were assessed using N_2 adsorption isotherms, as shown in Fig. 1(c) and Table 1. The CB and CgC31, which had a higher CB ratio, display a reversible type I adsorption isotherm, indicating high microporosity. In contrast, samples such as gC, CgC11, and CgC13 exhibited a hysteresis loop typical of type IV isotherms, suggesting the presence of mesopores. As indicated by the BJH plots in Fig. 1(d), gC, CgC11, and CgC13 exhibited mesopores with pore sizes ranging from 2 to 50 nm, whereas CB and CgC31 were microporous with pore sizes under 2 nm. The BET surface area and total pore volume of CgC31 are notably higher than those of gC alone, indicating that CB incorporation enhanced the available adsorption sites which further enhanced degradation. Moreover, in comparison to similar CP-based adsorbents reported in the literature, the specific surface area of Ti–CP was 445.018 $m^2\ g^{-1}$, while that of the CdS/g-C_3N_4/CP composite was 238.43 $m^2\ g^{-1}$. Therefore the Cu-BTC/g-C_3N_4 composite exhibited a competitive surface area, promoting higher adsorption efficiency and degradation.[46]

Table 1 Surface area, average pore size, and total pore volume of photocatalysts

Catalyst	Surface area ($m^2\ g^{-1}$)	Average pore size (nm)	Total pore volume ($cm^3\ g^{-1}$)
CB	1223.9	1.66	0.5098
gC	97.5	11.23	0.2735
CgC11	112.0	5.66	0.1585
CgC13	71.8	17.29	0.3104
CgC31	913.9	2.28	0.5202

3.1.4. XPS analysis. The elemental structure, oxidation states, and core electron binding energies were analyzed utilizing X-ray photoelectron spectroscopy (XPS). This method allowed the distinction between two binding energies related to metal ion spin–orbit splitting. The initial composite survey spectrum of the CgC31 composite, primarily composed of copper, oxygen, nitrogen, and carbon, is presented in Fig. 2(a). The spectra were successfully deconvoluted using a least-square Gaussian-fit model. In the Cu 2p spectrum, a peak at approximately 934.3 eV corresponded to Cu(II) in the Cu $2p_{3/2}$ state, while a peak at 954.9 eV was attributed to Cu(II) in the Cu $2p_{1/2}$ state, as shown in Fig. 2(b). Additionally, shake-up satellites were observed in

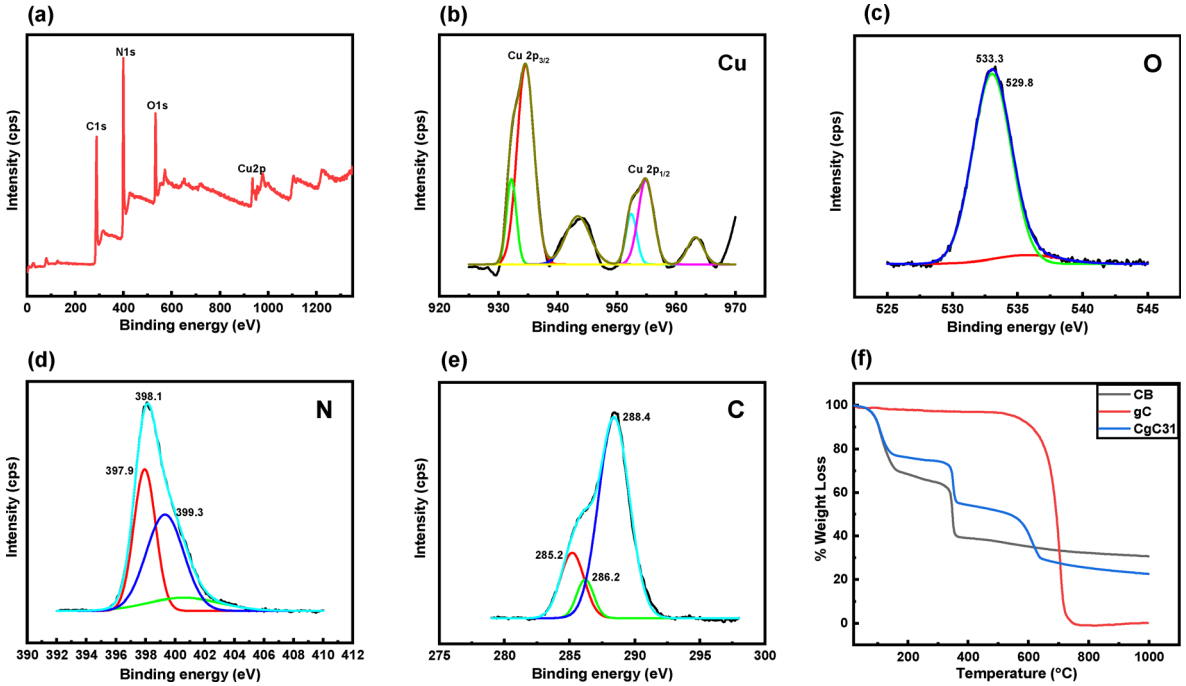

Fig. 2 XPS spectra of CgC31, (a) survey spectra, (b) Cu 2p, (c) O 1s, (d) N 1s, and (e) C 1s, and (f) TGA curves of CB, gC, and CgC31.

the 960–964 eV and 940–945 eV regions. The deconvoluted O 1s spectra in Fig. 2(c) revealed two peaks at 533.3 eV and 529.8 eV, corresponding to oxygen from water and BTC, respectively.

In Fig. 2(d), the nitrogen (N 1s) spectra displayed peaks corresponding to graphitic N, pyrrolic N, and pyridine N at 400.7 eV, 399.2 eV, and 398.7 eV, respectively. In the C 1s spectra in Fig. 2(e), a peak at 288.4 eV indicated the presence of BTC, while peaks at 286.2 eV and 285.2 eV corresponded to the C–H and C–C bonds. All results confirmed the successful synthesis of the CuBTC and g-C_3N_4 composite.[47,48]

3.1.5. Thermogravimetric analysis. Thermogravimetric analysis (TGA) was performed to evaluate the thermal stability of CB, gC, and their composite CgC31, as shown in Fig. 2(f). For g-C_3N_4, significant weight loss occurred between 600 and 750 °C due to carbon nitride decomposition.[49] CB showed initial water loss near 150 °C and further weight loss between 200 and 330 °C from the breakdown of its structure. The composite exhibited patterns from both materials, with water loss below 200 °C, CB decomposition around 350 °C, and final weight reduction at 550 °C due to gC degradation.

3.1.6. FESEM-EDS mapping and HRTEM analysis. The structural properties of the synthesized composite were examined using field emission scanning electron microscopy (FESEM). As illustrated in Fig. 3, the FESEM images of CB, gC, and the CgC31 composite revealed distinct morphologies. CB was characterized by an octahedral structure, while gC exhibited sheet-like formations. In the nanocomposite, both morphologies were observed, confirming the successful integration of CB and g-C_3N_4, and the construction of a heterojunction structure. The stoichiometric composition of the nanocomposite was determined through energy dispersive spectroscopy (EDS), which confirmed the presence of Cu, C, N, and O. Furthermore, elemental mapping demonstrated the homogeneous distribution of these elements, contributing to the enhanced photocatalytic activity of the composite. The HRTEM images of the synthesized nanocomposite revealed agglomerated particles within sheet-like structures, with three distinct sets of lattice fringes identified, corresponding to the (102), (100), and (003) crystallographic planes. The observed fringes showed d-spacing values of 0.53 nm and 0.367 nm, attributed to CB (2θ = 17.5°) and gC (2θ = 27.46°), respectively.

3.1.7. Photoluminescence (PL) analysis. Photoluminescence (PL) analysis was performed to assess charge carrier migration and recombination.[50] A decrease in PL intensity suggests minimized recombination, resulting in enhanced charge transfer and improved photocatalytic performance.[51] The PL spectra in Fig. 4(a), recorded at 320 nm, showed that pure CB and g-C_3N_4 had the highest PL intensities, while the CgC31 composite exhibited the lowest. This suggests more efficient charge segregation and transport in the composite, due to the formation of a heterojunction. As the CB content was increased, a further reduction in PL intensity was observed, suggesting that the majority of photogenerated charge carriers were derived from CB.

3.1.8. UV-vis DRS analysis. Diffuse reflectance spectroscopy (DRS) was used to analyze the light absorption capacity and band gap of the materials. As depicted in Fig. 4(b), significant UV light absorption was observed in the synthesized photocatalysts. While the bare CB material was inactive under UV light and only adsorbed pollutants, combining it with gC formed a composite that not only adsorbed but also degraded pollutants under UV irradiation. The band gap energy was

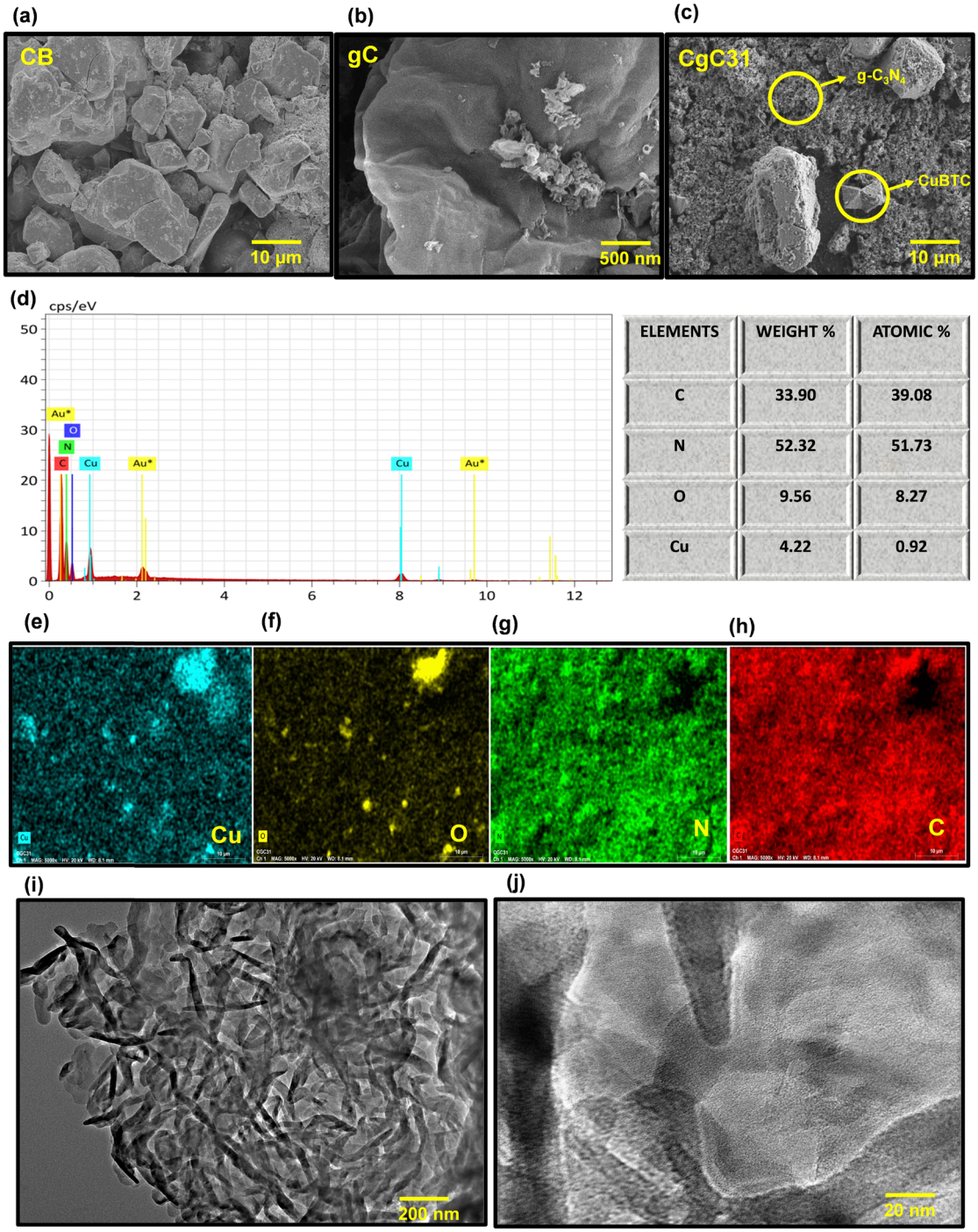

Fig. 3 FESEM images of (a) CB, (b) gC, (c) CgC31 composite, (d) EDS spectrum, (e)–(h) elemental mapping and (i) and (j) HRTEM images of the CgC31 heterojunction.

calculated utilizing a Tauc plot in Fig. 4(c), derived from the corresponding eqn 1.

$$(\alpha h\nu)^{\frac{1}{2}} = h\nu - E_g \quad (1)$$

In this equation, the variables h, ν, α, and E_g represent Planck's constant, light frequency, absorption coefficient, and band gap energy, respectively. The band gap was determined where the linear portion of the plot intersects the x-axis.[52] The calculated band gaps for CB, g-C_3N_4, CgC11, CgC13, and CgC31 photocatalysts were 1.85, 3.07, 3.05, 2.97, and 2.92 eV, respectively. Despite CB having the lowest band gap, it remained photo catalytically inactive, serving primarily as an adsorbent, while its composite with g-C_3N_4 especially CgC31 exhibited enhanced photocatalytic degradation under UV light due to the effective heterojunction formation and synergistic charge separation.

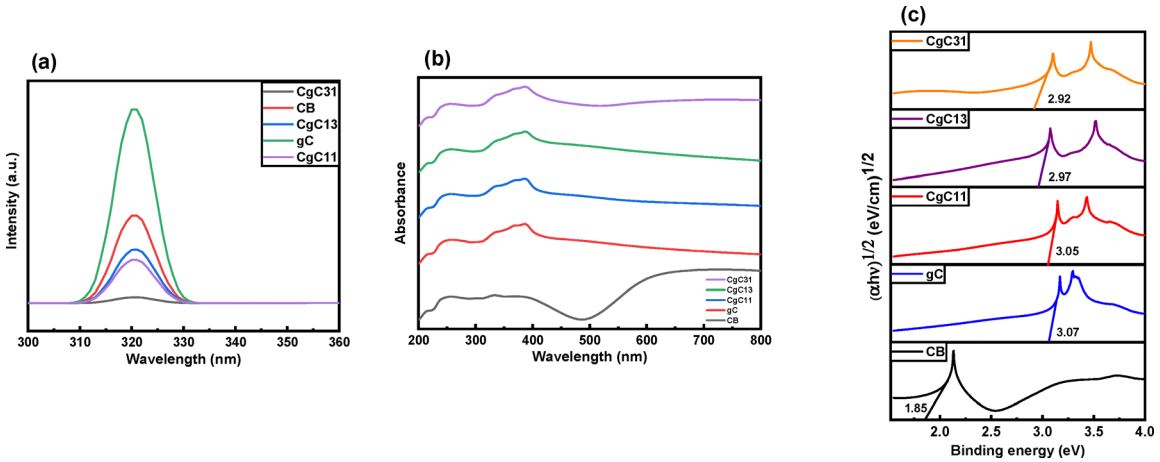

Fig. 4 (a) PL spectra, (b) UV-Vis DRS spectra, and (c) Taucs plot of CB, g-C_3N_4, CgC11, CgC13, and CgC31.

3.1.9. EIS analysis. EIS analysis was conducted to assess the charge transfer efficiency of CB, g-C_3N_4, and the nanocomposite. A reduced arc radius in the Nyquist plot indicates improved charge separation and enhanced interfacial charge transport.[53] The observed arc radii followed the order: g-C_3N_4 > CB > CgC31. As shown in Fig. S1 (ESI†), the incorporation of CB and g-C_3N_4 led to a reduction in the arc radius, demonstrating lower electron transfer resistance and minimized electron–hole recombination. The CgC31 composite showed the smallest arc radius, signifying superior conductivity and faster charge migration, which aligns with the PL analysis showing enhanced charge separation.

3.2. Impact of the catalyst dose

The effectiveness of photocatalysis heavily depends on using the optimal catalyst amount. Too much catalyst can lead to particle aggregation, reducing efficiency. Using the right dosage maximizes photon absorption and promotes efficient degradation. Tests with catalyst concentrations from 0.1 g L^{-1} to 0.6 g L^{-1} in Fig. 5(a) showed that degradation efficiency decreased beyond

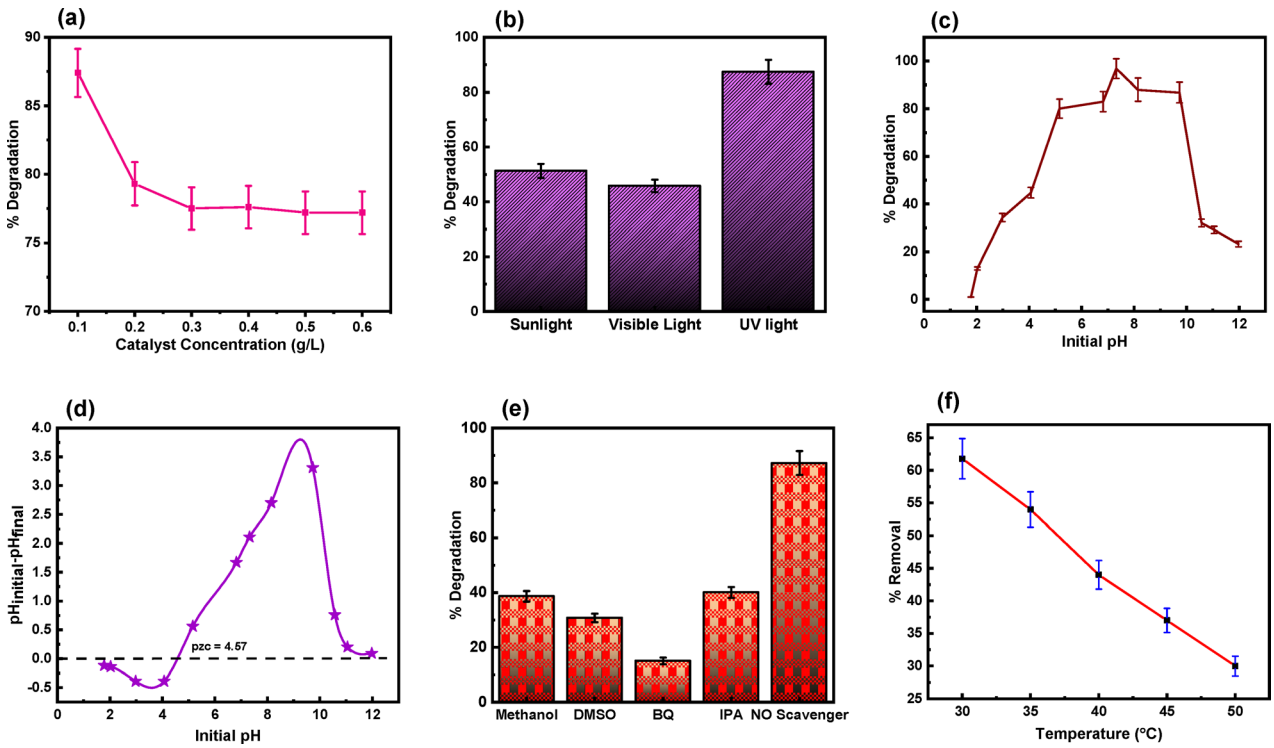

Fig. 5 Impact of (a) catalyst dose, (b) various lights, (c) pH, (d) pzc studies, (e) scavengers, and (f) temperature. Error bars represent the standard deviation from triplicate experiments with 95% confidence intervals.

0.1 g L^{-1} due to increased opacity, which scattered light and limited its impact on the solution. Additionally, the catalyst surface became saturated, offering no further improvement in degradation. Thus, 0.1 g L^{-1} was identified as the optimal concentration for future experiments.

3.3. Impact of various lights

Comparative photocatalytic experiments under UV, visible, and natural sunlight were conducted to assess pollutant degradation. As shown in Fig. 5(b), decomposition reached 51.3% under sunlight and 45.8% when exposed to visible light, while the highest removal rate of 87.4% was achieved when exposed to UV light using the CgC31 heterojunction photocatalyst. These results highlight the superior effectiveness of UV light in driving pollutant degradation with the developed photocatalyst, making it more efficient.

3.4. Impact of pH

pH plays a crucial role in controlling photocatalyst degradation efficiency, as it influences adsorption capacity, surface charge, and the ionization state of the catalyst.[54] The photocatalyst's point of zero charge (PZC) was determined to be 4.57 in Fig. 5(d). Below pH 4.57, the surface is positively charged, and above it, negatively charged. Tetracycline (TC) exhibits different ionic forms depending on the pH due to its multiple p*K*a values (3.3, 7.7, 9.7, and 10.7). At pH $<$ 3, TC is positively charged, while at pH $>$ 7.7, it becomes anionic. TC is in a zwitterionic form in the pH range of 3.3–7.7.[55] The degradation efficiency of TC by the CgC31 photocatalyst was lower in highly acidic or basic environments due to repulsive interactions between the ionic forms of TC and the charged catalyst surface. However, at pH 7, where TC is in its zwitterionic form, the electrostatic affinity between TC and the negatively charged photocatalyst surface enhanced degradation, achieving maximum removal efficiency (96.8%) under neutral to alkaline conditions in Fig. 5(c). This highlights the photocatalyst's optimal performance in real-world applications.

3.5. Impact of temperature

The effect of temperature on tetracycline removal using CgC31 is shown in Fig. 5(f). Experiments conducted between 30 °C and 50 °C revealed a decrease in removal efficiency with increasing temperature, indicating an exothermic adsorption process. The highest removal was achieved at 30 °C, where TC molecules gained sufficient energy for adsorption. At higher temperatures, weakened electrostatic interactions caused a shift towards desorption. Therefore, 30 °C was chosen as the optimal temperature for the adsorption experiments. The temperature range (25–50 °C) was selected to evaluate the thermal effects on adsorption under conditions relevant to practical wastewater treatment. This range captures the influence of moderate thermal fluctuations on adsorption efficiency, as excessive temperatures may lead to material degradation or altered adsorption mechanisms.[45]

3.6. Adsorption isotherms

The fundamental equations and theoretical framework of adsorption isotherms are provided in the ESI.†

The adsorption data were first analyzed using the Langmuir isotherm model, which assumes monolayer adsorption on a homogeneous CgC31 surface. Here, Q_m represents the maximum adsorption capacity or the highest amount of tetracycline adsorbed per gram of CgC31 (mg g^{-1}).[56] The Langmuir constant, K_L (L mg^{-1}), reflects binding efficiency and was used to calculate the separation factor (R_L). Fig. 6(a) inset shows that R_L decreases as the initial concentration (C_0) increases, with $0 < R_L < 1$ confirming favorable adsorption.

The Freundlich isotherm describes adsorption on heterogeneous surfaces in layers. An n value above 1 indicates effective sorption, and the Freundlich constant, approximately 3.546, suggests a suitable adsorption mechanism, while a $1/n$ value between 0 and 1 further supports favourable adsorption.[57] The Freundlich plot is shown in Fig. 6(b). The Dubinin–Radushkevich (D–R) model, based on Polanyi's theory, indicates non-uniform adsorption, with an average adsorption energy (E) of 0.3429 kJ mol^{-1}, suggesting physisorption in Fig. 6(c). The Temkin isotherm, seen in Fig. 6(e), proposes that the adsorption heat decreases as bonding increases between the adsorbate and the adsorbent. With β representing maximum bond energy, BT = RT/β was calculated at 10.22 kJ mol^{-1}, indicating physical adsorption.[58] The Harkins–Jura and Halsey in Fig. 5(e and f) isotherms illustrate heterogeneous pore distribution and multilayer adsorption. The Langmuir isotherm with the highest R^2 value indicates monolayer adsorption on CgC31, while the D–R model confirms an uneven adsorbent surface.[59] To further validate the model accuracy, statistical error values were calculated, where the Langmuir model exhibited the lowest χ^2 (0.288) confirming its superior fit compared to the other models. These findings indicate monolayer adsorption as the dominant mechanism, consistent with previous studies (Table 2).[60]

3.7. Adsorption kinetics

The primary equations and theoretical framework for adsorption kinetics are detailed in the ESI.† The parameters and coefficients for the pseudo-first-order, pseudo-second-order, intraparticle diffusion, Elovich, and liquid film models are summarized in Table 3. A satisfactory correlation with the experimental data is observed across all models, with the pseudo-first-order kinetic model showing the highest fit (R^2 = 0.96075) with 95% confidence intervals for the adsorption of tetracycline onto CgC31, suggesting that the rate of tetracycline adsorption onto CgC31 is primarily governed by the initial concentration of tetracycline in the solution, reflecting a surface-driven interaction. Additionally, strong correlations with intraparticle diffusion (R^2 = 0.93594) and liquid film models (R^2 = 0.96075) as compared to the other models as pseudo-second-order (R^2 = 0.88119) and Elovich model (R^2 = 0.89516) with similar confidence ranges suggest that both internal particle diffusion and boundary layer effects contribute significantly to the adsorption efficiency of tetracycline onto CgC31, highlighting a multi-step adsorption pathway (Fig. 7).[61]

3.8. Photocatalytic degradation kinetics

The photocatalytic degradation dynamics of the antibiotic were assessed by monitoring its concentration *via* UV-vis

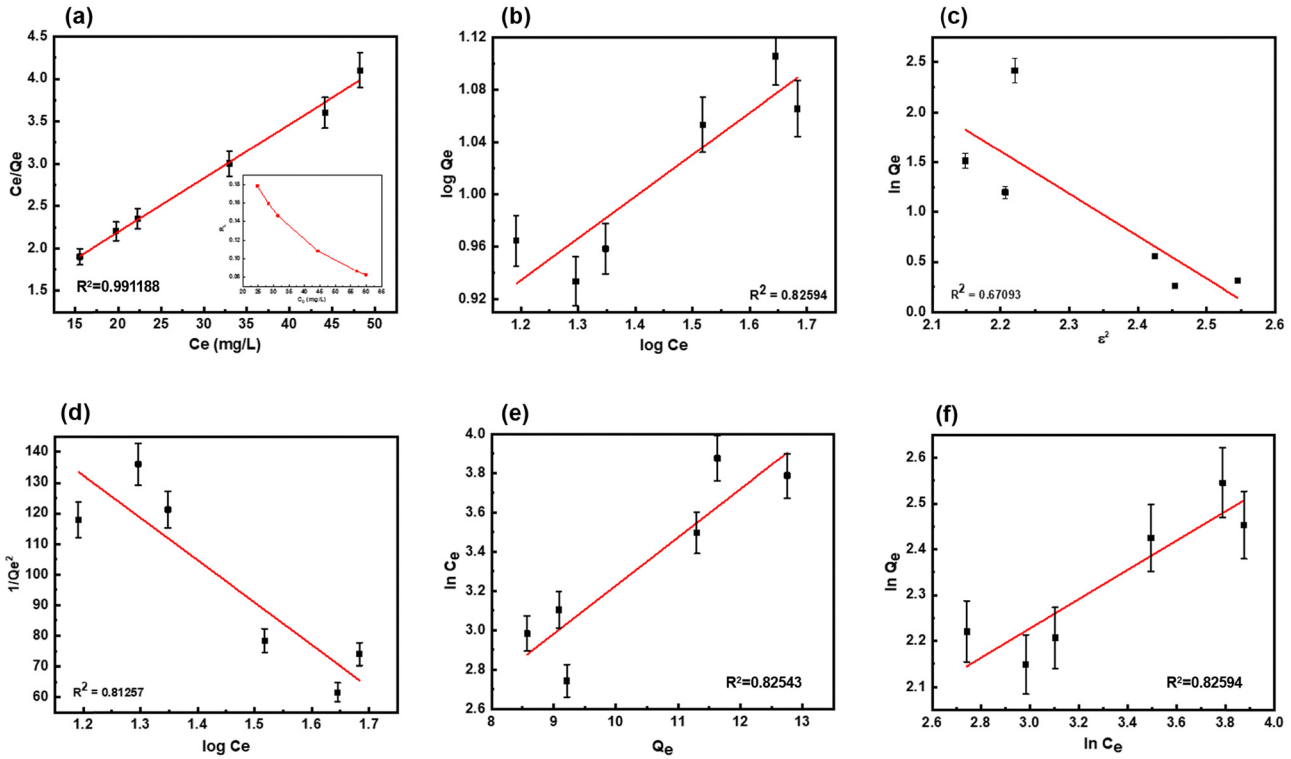

Fig. 6 Linearly fitted adsorption isotherm plots for (a) Langmuir (inset RL plot), (b) Freundlich, (c) D–R model, (d) Harkins–Jura, (e) Temkin, and (f) Halsey. Error bars represent the standard deviation from triplicate experiments. The 95% confidence intervals for the best-fitting model are shown.

spectrophotometry, providing degradation rate and time data, with fundamental equations detailed in the ESI.† The kinetic analysis indicates that the degradation process aligns closely with pseudo-first-order kinetics, as evidenced by an R^2 value near unity with a rate constant of k = 0.02098 min^{-1}. This suggests that the reaction rate is primarily dependent on the concentration of the tetracycline pollutant, highlighting the efficiency of the composite in facilitating rapid degradation. The efficiency of various photocatalysts, including CB, gC, CgC11, CgC13, and TiO2-P25, was compared in a series of same experiments. The results revealed that CgC31 outperformed the others, exhibiting a rate constant of 0.02098, which was significantly higher than those of CB (1×10^{-16} min^{-1}), gC (0.0038 min^{-1}), TiO_2-P25 (0.0062 min^{-1}), CgC11 (0.003 min^{-1}), and CgC13 (0.004 min^{-1}). A synergy factor (R) was calculated using the below eqn (2) to assess the enhanced performance of the composite materials.

$$R = \frac{k_{CB+gC}}{k_{CB} + k_{gC}} \quad (2)$$

This factor was derived using the photodegradation rate constants of the CB/gC composite and its components. The highest synergy factor of 5.53 was observed for CgC31 as compared to 0.789 for CgC11 and 1.053 for CgC13 which correlated with its superior photocatalytic degradation efficiency.[62] The enhanced photocatalytic activity of the CgC31 composite can be attributed to the synergistic effects between Cu-BTC's high surface area and porosity and g-C_3N_4's electronic properties. Cu-BTC provides abundant active sites for adsorption, while gC facilitates charge transfer, reducing electron–hole recombination and improving photocatalytic efficiency. The intimate interfacial contact between the two materials enhances charge separation and strengthens adsorption interactions, leading to superior dye removal performance.[63] This is further supported by literature findings on charge transfer dynamics in similar heterojunction systems.[61]

3.9. Thermodynamic studies

The thermodynamic analysis of tetracycline removal onto CgC31 indicates that the process is spontaneous at lower temperatures (303 K), as shown by the negative Gibbs free energy (ΔG° = −0.0927 kJ mol^{-1}). However, at higher temperatures (308–323 K), ΔG° becomes positive suggesting reduced adsorption efficiency. A more negative ΔG with increasing temperature suggests enhanced feasibility of adsorption at higher temperatures. The negative enthalpy change (ΔH° = −64.8359 kJ mol^{-1}) confirms that adsorption is exothermic, indicating strong interactions between tetracycline molecules and CgC31. Since adsorption releases heat, higher temperatures may reduce adsorption efficiency by shifting equilibrium toward desorption making the process more favorable at lower temperatures. The positive entropy change (ΔS° = 0.214286 J mol^{-1} K^{-1}) suggests increased disorder at the solid–liquid interface, likely due to tetracycline molecules displacing water molecules on the adsorbent surface. However, as temperature increases, ΔS° slightly decreases, indicating a reduction in

Table 2 Adsorption isotherm parameters for tetracycline adsorption on CgC31

Equilibrium isotherms	Equation	Parameters	Values
Langmuir	$\frac{C_e}{q_e} = \frac{1}{Q_m K_L} + \frac{1}{Q_m} C_e$	Q_m (mg g^{-1})	15.74
		K_L (L mg^{-1})	0.069
		R^2	0.99188
		X^2	0.288 best fit
Freundlich	$q_e = K_F C_e^{1/n}$	K_F [(mg g^{-1}).(L mg^{-1})$^{1/n}$]	3.546
		$1/n$	0.3204
		R^2	0.82594
		X^2	1 428 081 very high
Freundlich	$q_e = K_F C_e^{1/n}$	K_F [(mg g^{-1}).(L mg^{-1})$^{1/n}$]	3.546
		$1/n$	0.3204
		R^2	0.82594
		X^2	1 428 081 very high
D–R model	$\ln q_e = \ln Q_s - B\varepsilon^2$	Q_S (mg g^{-1})	57 411.65
		B [(mol J^{-1})^2]	4.25
		E (kJ mol^{-1})	0.3429
		R^2	0.67093
		X^2	NA
Harkins–Jura	$\frac{1}{q^2 e} = \left(\frac{B}{A}\right) - \frac{1}{A}\log C_e$	A	0.00723
		B	2.156
		R^2	0.81257
		X^2	6188.36 very poor fit
Temkin	$q_e = B_T \ln K_T + B_T \ln C_e$	B_T	0.24626
		K_T (L mg^{-1})	22.309
		B (J mol^{-1})	10 220.86
		R^2	0.82543
		X^2	299.6 moderate fit
Halsey isotherm	$\ln q_e = \frac{1}{n}\ln K - \frac{1}{n}\ln C_e$	N	−3.121
		K (mg L^{-1})	51.96
		R^2	0.82594
		X^2	670.61

Table 3 Adsorption and degradation kinetic parameters

Kinetic model	Equations	Parameters	Values
Adsorption kinetics			
Pseudo-first-order	$-\ln\left(1 - \frac{q_t}{q_e}\right) = k_1 t$	k_1 (min^{-1})	0.03565
		Q_e (mg g^{-1})	2.4622
		R^2	0.96075
Pseudo-second-order	$\frac{t}{q_t} = \frac{1}{k^2 q_e^2} + \frac{t}{q_e}$	k_2 (min^{-1})	0.03397
		Q_e (mg g^{-1})	0.3956
		R^2	0.88119
Intra-particle diffusion	$q_t = k_1 t^{\frac{1}{2}} + C_1$	K_1 (min^{-1})	0.02541
		C_1 (mg g^{-1})	0.03029
		R^2	0.93594
Elovich model	$q_t = \frac{1}{\beta}\ln(\alpha\beta) + \frac{1}{\beta}\ln(t)$	a (mg g^{-1} min^{-1})	0.6485
		b (g mg^{-1})	11.88
		R^2	0.89516
Liquid-film model	$-\ln(1 - F) = K_{fd} \times t$	K_{fd}	0.0356
		R^2	0.96075
Degradation kinetics			
Pseudo-first-order	$\ln(C_t) = \ln(C_0) - k_1 t$	k_1 (min^{-1})	0.02098
		R^2	0.99268
Pseudo-second-order	$\frac{t}{C_t} = \frac{1}{k_2 C_0^2} + \frac{t}{C_0}$	k_2	0.2729
		R^2	0.90586

randomness. These findings highlight that tetracycline adsorption is thermodynamically favorable at moderate temperatures, but higher temperatures reduce its efficiency due to the increasing ΔG°.[64] The theory, equations, and plot provided in Fig. S2 and Table S1 (ESI†) were used for the thermodynamic calculations.

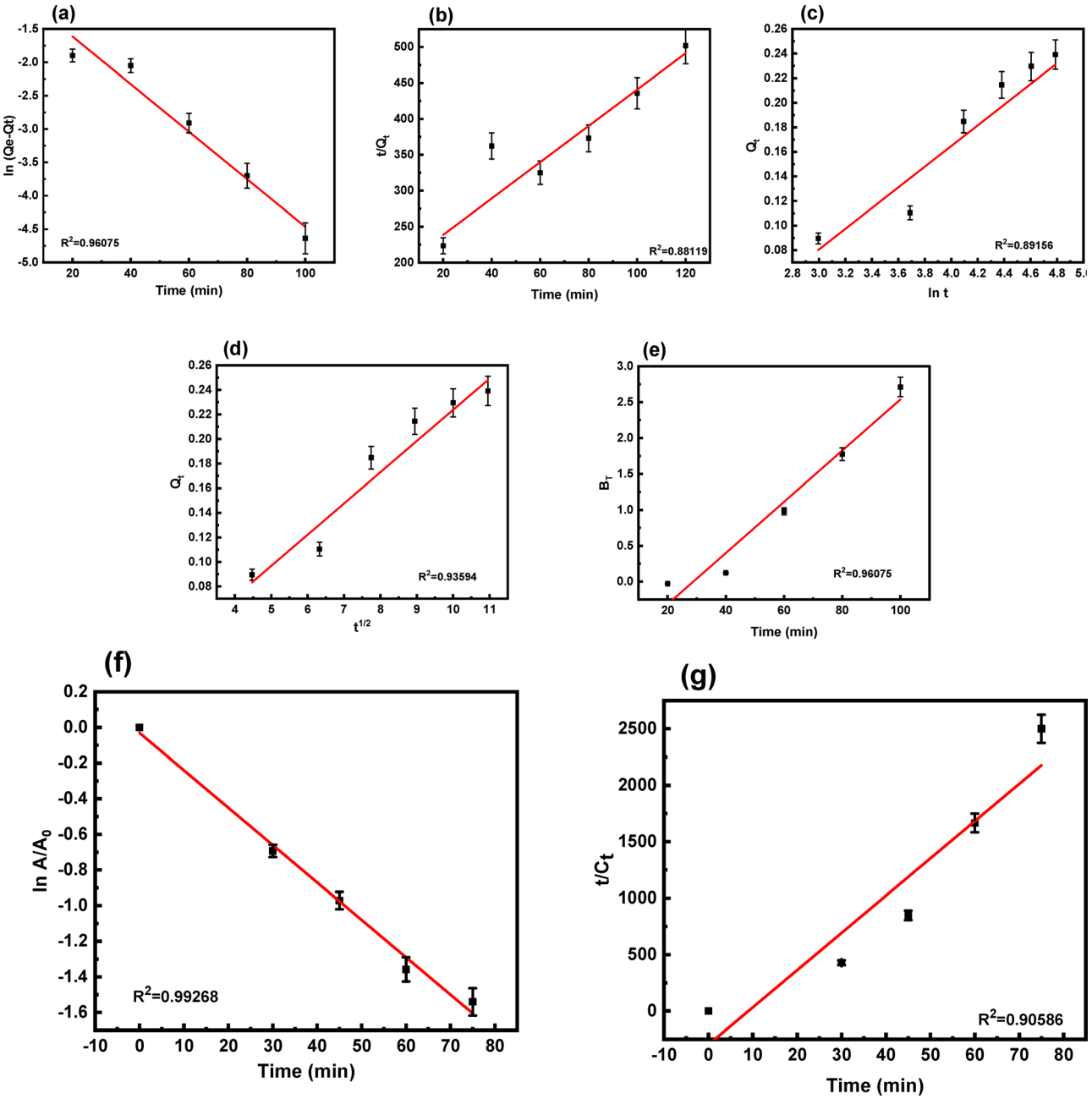

Fig. 7 Linearly fitted adsorption kinetic plots for (a) pseudo-first-order, (b) pseudo-second-order, (c) Elovich, (d) intraparticle diffusion, and (e) liquid film models and degradation kinetic plots for (f) pseudo-first-order and (g) pseudo-second-order models. Error bars represent the standard deviation from triplicate experiments. The 95% confidence intervals for the best-fitting model are shown.

3.10. Possible adsorption and photocatalytic mechanism with the effect of scavengers

The adsorption mechanism of the CB/g-C_3N_4 composite for tetracycline hydrochloride can be explained through a combination of potential interactions including hydrogen bonding, pore filling, π–π interactions, van der Waals forces, and electrostatic interactions. The presence of hydroxyl and carboxyl groups on the composite surface suggests that hydrogen bonding with tetracycline's polar functional groups likely plays a significant role in adsorption.

Additionally, the porous nature of CB/gC, observed through BET surface area analysis, points toward pore-filling as an effective means of trapping tetracycline molecules within the composite's structure. The π–π interactions between the aromatic rings of tetracycline and the composite could also contribute to the composite's affinity for the antibiotic, aligning with observed trends in adsorption studies of similarly structured pollutants.

Electrostatic forces may influence adsorption as well, given that the pH of the solution affects both the composite's charge

and tetracycline's ionization state, which can favor attraction or repulsion based on the pH. These combined mechanisms suggest that the Cu-BTC/g-C_3N_4 composite leverages multiple types of interactions for effective adsorption of tetracycline, confirming its potential as a versatile adsorbent for environmental remediation.

The energy levels of the valence band (VB) and the conduction band (CBT) were determined using eqn (3) and (4) provided below.

$$E_{VB} = X - E_e + 0.5E_g \quad (3)$$

$$E_{CBT} = E_{VB} - E_g \quad (4)$$

In these equations, E_{CBT} and E_{VB} denote the energies of the conduction band and the valence band, respectively. X signifies the compound's electronegativity, while E_e is the electron energy relative to hydrogen, which is set at 4.5 eV.

The E_{CBT} values for CB and g-C_3N_4 were determined to be 0.52 eV and −0.99 eV, respectively, while their corresponding E_{VB} values were determined to be 2.37 eV and 2.08 eV, respectively.[65,66]

The degradation process is primarily driven by electrons in the conduction band (CBT) and holes in the valence band (VB), along with reactive species such as superoxide and hydroxyl radicals, which are the key players.[67] A scavenger study determined the predominant species involved in the degradation mechanism. Various scavengers were utilized, including dimethyl sulfoxide (DMSO), methanol, benzoquinone (BQ), and isopropyl alcohol (IPA), to selectively quench electrons (e^-), holes (h^+), superoxide radicals ($O_2^{\bullet -}$), and hydroxyl radicals ($OH^\bullet$), respectively.[52] In the absence of any trapping agents, the antibiotic underwent 87.2% degradation. However, the addition of scavengers to the reaction medium significantly suppressed the photocatalytic degradation rate. The comparable inhibition effects observed in Fig. 5(e) for all scavengers suggest that multiple reactive species, including holes, electrons, superoxide radicals, and hydroxyl radicals, were actively involved but superoxide radicals contributed the most to the degradation process.

So upon exposure to light, electrons within the valence bands of the semiconductors become excited and transition to their respective conduction bands. When the semiconductors are in close proximity, holes migrate from the more positively charged valence band of CB to the less positively charged valence band of gC, effectively inhibiting the recombination of photogenerated charge carriers. Concurrently, electrons transfer from the more negatively charged conduction band of gC to the less negatively charged conduction band of CB. Within CB's conduction band, these electrons participate in the reduction of oxygen to produce $O_2^\bullet$, which subsequently reacts with water to generate $^\bullet OH$ radicals. These oxidative species effectively degrade TC into H_2O, CO_2, and other less toxic products. Additionally, the holes in the valence band of g-C_3N_4 react with water to produce $OH^\bullet$ radicals, further oxidizing pollutants into simpler compounds. The effective separation of electron–hole pairs and the reduction of recombination greatly improve the photocatalytic performance of the CgC31 composite, as depicted in Scheme 3. The possible reaction steps are presented in the following equations.

$$CB/gC + h\nu \rightarrow e^- + h^+ \quad (5)$$

$$e^-_{CBT} + O_2 \rightarrow O_2^{-\bullet} \quad (6)$$

$$O_2^{-\bullet} + H_2O \rightarrow HOO^\bullet + OH^\bullet \quad (7)$$

$$h^+_{VB} + OH^- \rightarrow OH^\bullet \quad (8)$$

$$OH^\bullet/h^+ + \text{pollutant} \rightarrow \text{degraded products} \quad (9)$$

3.11. Mineralization studies

The intermediates formed during the photodegradation of organic dyes were identified by measuring total organic carbon (TOC) and chemical oxygen demand (COD) during irradiation. After 60 minutes of UV light exposure, TOC and COD reduction efficiencies for TC were observed to be 67.8% and 68.6%, respectively. As shown in Fig. 8(a), the solution was mineralized, with the remaining intermediates exhibiting low mineralization potential. The formation of intermediate organic compounds during the process, before complete conversion of TC into CO_2 and simpler byproducts, led to a lower percentage of TOC and COD removal compared to the degradation rate.

3.12. Probable degradation pathway of tetracycline

The products and the intermediates generated during the photocatalytic degradation of tetracycline (TC) were analyzed using LC-MS. The corresponding mass spectra are presented in Fig. S3 (ESI†). The degradation process was found to proceed *via* three distinct pathways, as illustrated in Scheme 2. In pathway I, the first intermediate, product 1 (m/z = 462), undergoes further decomposition, yielding two secondary intermediates: product 2 (m/z = 434) and product 3 (m/z = 478). These intermediates lead to the formation of additional minor intermediates and ring-opened byproducts as the reaction progresses. Pathway II begins with the formation of product 8 (m/z = 434) through the loss of an *N*-methyl group, resulting from the cleavage of the N–C bond. This intermediate subsequently undergoes ring cleavage and dehydroxylation *via* oxidation by hydroxyl radicals, leading to the formation of product 9 (m/z = 304). In pathway III, product 11 (m/z = 475) is formed *via* a 1,3-dipolar cycloaddition at the double bond, followed by a rearrangement and oxidation by hydroxyl radicals. Product 11 is then converted to product 12 (m/z = 437) through N–C bond cleavage and hydroxyl substitution reactions. Further degradation transforms product 12 into product 13 (m/z = 210) *via* the loss of methyl and hydroxyl groups and the cleavage of the C–C bond, leading to the breakdown of rings. Subsequent oxidation of products 9 and 13 generates product 10, which is identified as the final intermediate before complete mineralization. The degradation process ultimately results in the production of simpler byproducts, primarily CO_2 and H_2O, completing the mineralization of TC (Scheme 3).

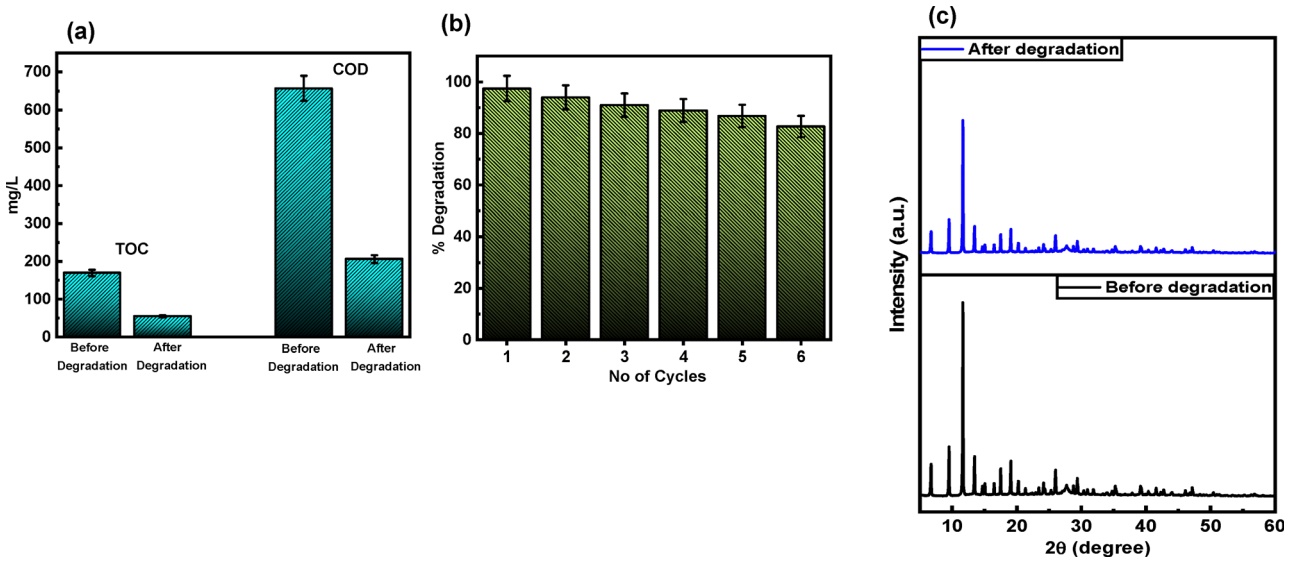

Fig. 8 (a) TOC and COD values of tetracycline before and after degradation, (b) reusability studies and (c) XRD of CgC31 before and after degradation.

3.13. Reusability studies

Evaluating the durability of a photocatalyst is essential for its practical application. To assess the repeatability and photostability of the CgC31 photocatalyst, recycling experiments were conducted under identical conditions to observe the photodegradation of TC over multiple cycles. Following each cycle, the catalyst was separated using centrifugation, cleaned, dried, and then reused in subsequent cycles. As illustrated in Fig. 8(b), after six cycles, the degradation efficiency remained around 80%, confirming the reusability of CgC31. The reduction in efficiency from 97.4% to 82.7% may be attributed to catalyst loss during recovery and the accumulation of untreated intermediates on the surface, which could block pores and active sites. Furthermore, the structural stability of the CgC31 catalyst was confirmed through XRD analysis after six cycles (Fig. 8(c)), indicating that the positions and intensities of the diffraction peaks remained consistent, with no additional peaks observed, confirming the preservation of the crystal structure. Hence, this

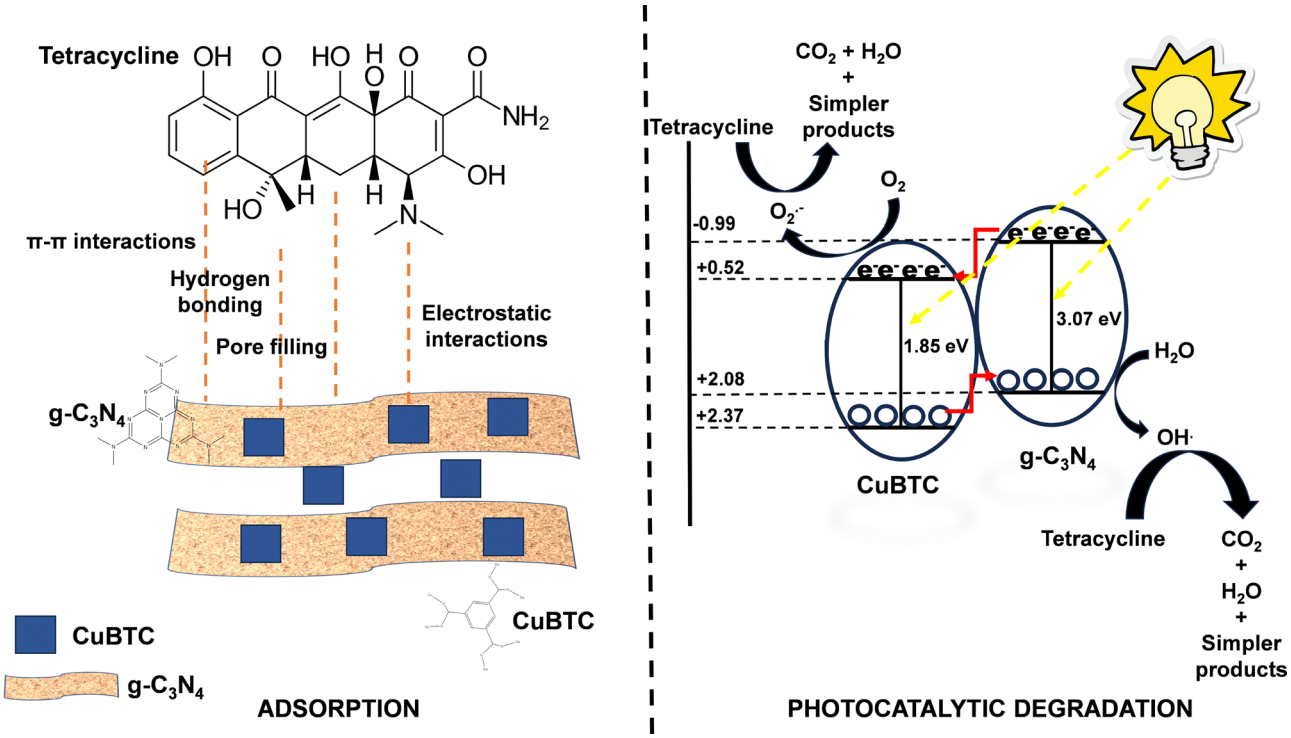

Scheme 2 Possible adsorption and photocatalytic mechanism.

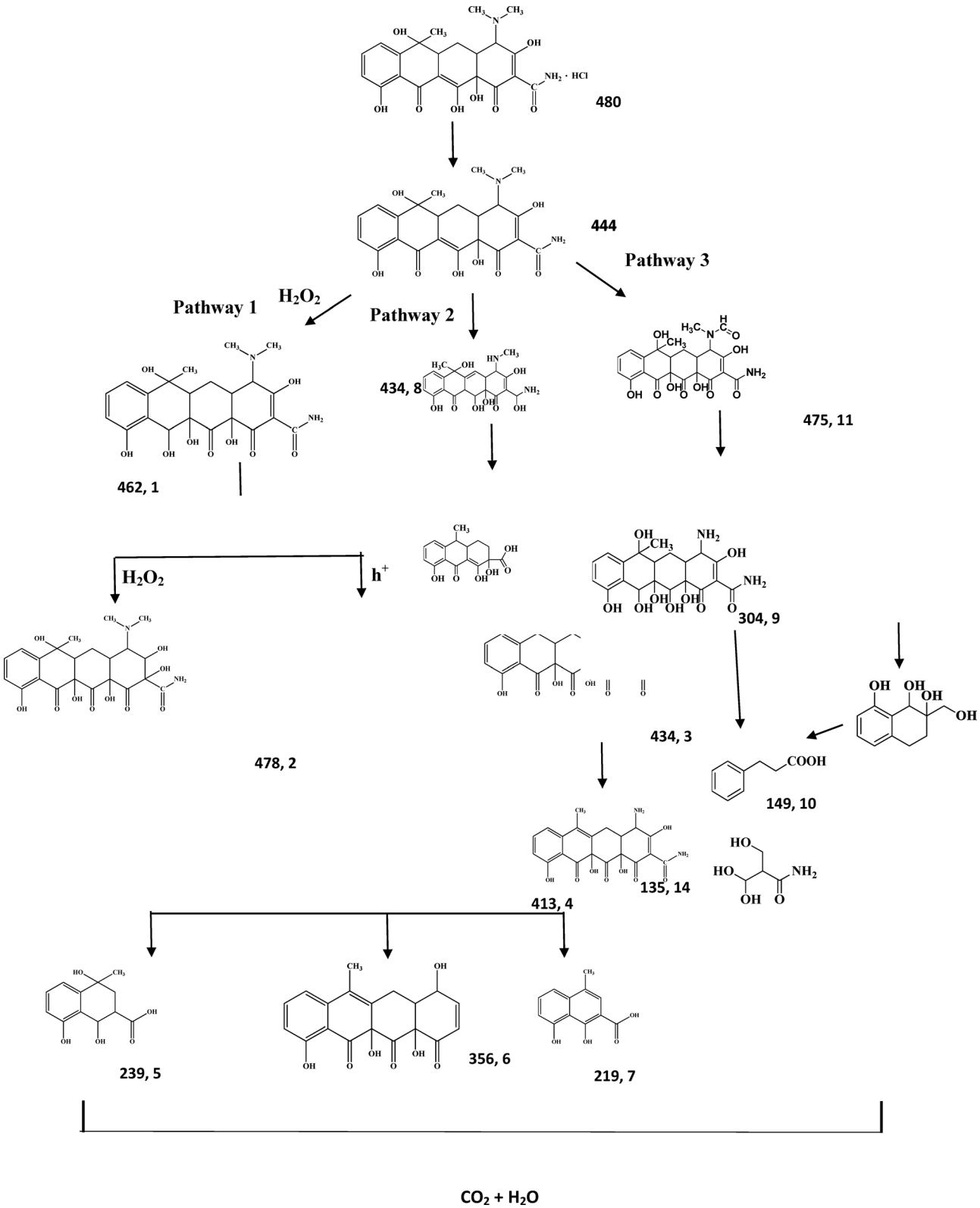

Scheme 3 Potential photocatalytic reaction route of TC using the CgC31 photocatalyst.

promising adsorption and photocatalytic performance of our composite suggest its potential application in wastewater treatment plants for the removal of antibiotic contaminants. Its dual-functionality—adsorption and photocatalysis—allows for effective tetracycline degradation under UV light conditions, making it energy-efficient compared to conventional

Table 4 Contrast with different photocatalysts for tetracycline degradation

Photocatalyst	Dose (g L^{-1})	Initial concentration of TC (ppm)	% Degradation	Time (min)	Ref.
Bi_2O_3/Sb_2S_3	0.3	10	91.5	120	68
g-C_3N_4/Sb_2S_3	0.2	5	99	120	53
$Sb_2S_3/ZnIn_2S_4$	0.3	10	85.36	140	69
$BiVO_4/Sb_2S_3$	0.3	10	88.7	120	70
TiO_2/GO	0.6	20	90	240	71
CB/g-C_3N_4	0.1	25	97.4	60	Present work

photocatalysts like TiO_2. Additionally, its structural stability over multiple cycles indicates feasibility for long-term use in real-world treatment systems. Future studies could explore scaling up the composite for efficient removal of contaminants like heavy metals, antibiotics, dyes and other organic pollutants. The composite can be incorporated into advanced filtration systems in industrial wastewater plants.

As shown in Table 4, our catalyst surpasses previously reported studies, demonstrating exceptional effectiveness even at lower dosages. The CB and gC combination stands out, achieving remarkable results in this work.

4. Conclusion

This study introduces an innovative CB/gC heterojunction photocatalyst synthesized *via* a sustainable hydrothermal approach, designed for effective antibiotic removal, particularly tetracycline, from wastewater. Characterization techniques including XRD, XPS, FE-SEM-EDS, TGA, BET, EIS, FTIR, HRTEM, UV-DRS, and PL validated the successful synthesis, structure, and stability of the composite. SEM imaging highlighted the seamless integration of gC onto CB, forming a heterojunction with enhanced light absorption and significant surface area. The CB/gC composite exhibited exceptional photocatalytic performance, achieving 97.4% degradation of 25 ppm tetracycline within 60 minutes under UV light. The degradation follows a pseudo-first-order reaction with a rate constant of 0.02098, which is 2.1 × 10^{14} times higher than that of pure CB and 5.5 times higher than that of pure gC_3N_4. This demonstrates strong synergy in the composite. Notably, the rate constant is 3.39 times greater than that of the commercial TiO_2-P25 photocatalyst. Key parameters such as the catalyst dose, pollutant concentration, pH, light sources, and scavenger analysis were systematically optimized, revealing the dominant roles of •OH radicals, electrons, holes, and superoxide species in driving the degradation pathway. Notably, the catalyst demonstrated high reusability, maintaining over 82.7% degradation efficiency across six cycles. Post-use XRD analysis confirmed its structural resilience, while TOC and COD measurements indicated substantial reductions of 67.8% and 68.6%, respectively, reflecting effective pollutant mineralization. Degradation intermediates and products were mapped using LC-MS, offering insights into the degradation mechanism. This study establishes CB/gC as a powerful, sustainable solution for antibiotic remediation, with potential for broader applications in solar-driven environmental purification, positioning it as a robust tool for addressing water pollution challenges. However, one potential challenge in practical applications is that the presence of other contaminants in industrial wastewater may lead to pore blockage or surface fouling, potentially affecting the photocatalytic efficiency. However, this can be mitigated by optimizing pretreatment steps or periodic regeneration of the catalyst to maintain long-term performance. Also, the absence of ESR analysis limits the direct identification of reactive species.

Author contributions

Palkaran Sethi: designed and performed the experiments, analyzed data, and co-wrote the paper. Soumen Basu: supervised the research, designed experiments and co-wrote the paper. Sanghamitra Barman: supervised the research, designed experiments, and co-wrote the paper.

Data availability

The data supporting the findings of this study, including characterization results, adsorption and degradation kinetics, and isotherm studies, are available in the article as well as in the ESI† provided with this article.

Conflicts of interest

The authors declare that they have no known competing financial interests or personal relationships that could have appeared to influence the work reported in this paper.

Acknowledgements

The authors would like to acknowledge Thapar Institute of Engineering and Technology for XRD, FESEM, and FTIR. The authors are also grateful to Dr Akansha Mehta, Fun Glass, Alexander Dubcek University, Slovakia for XPS analysis and Panjab University, Chandigarh, for HRTEM analysis.

References

1 N. Zhang, X. Ning, J. Chen, J. Xue, G. Lu and H. Qiu, Photocatalytic degradation of tetracycline based on the highly reactive interface between graphene nanopore and TiO_2 nanoparticles, *Microporous Mesoporous Mater.*, 2022, **338**, 111958.

2 Z. Yang, Q. Zhao, J. Gan, J. Zhang, M. Chen and Y. Zhu, Damage evolution characteristics of siliceous slate with

varying initial water content during freeze-thaw cycles, *Sci. Total Environ.*, 2024, **950**, 175200.
3 S. Chu, M. Lin, D. Li, R. Lin and S. Xiao, Adaptive reward shaping based reinforcement learning for docking control of autonomous underwater vehicles, *Ocean Eng.*, 2025, **318**, 120139.
4 Y. Yao, Y. Luo, Y. Yang, H. Sheng, X. Li and T. Li, *et al.*, Water free anaerobic co-digestion of vegetable processing waste with cattle slurry for methane production at high total solid content, *Energy*, 2014, **74**, 309–313.
5 S. Pal, Z. Ahamed and P. Pal, Removal of antibiotics and pharmaceutically active compounds from water Environment: Experiments towards industrial scale up, *Sep. Purif. Technol.*, 2022, **295**, 121249.
6 S. Pal, Z. Ahamed and P. Pal, Removal of antibiotics and pharmaceutically active compounds from water Environment: Experiments towards industrial scale up, *Sep. Purif. Technol.*, 2022, **295**, 121249.
7 A. H. Ragab, N. F. Gumaah, A. A. El Aziz Elfiky and M. F. Mubarak, Exploring the sustainable elimination of dye using cellulose nanofibrils- vinyl resin based nanofiltration membranes, *BMC Chem.*, 2024, **18**(1), 121.
8 K. Li, S. Zou, G. Jin, J. Yang, M. Dou and L. Qin, *et al.*, Efficient removal of selenite in aqueous solution by MOF-801 and Fe_3O_4/MOF-801: Adsorptive behavior and mechanism study, *Sep. Purif. Technol.*, 2022, **296**, 121384.
9 W. Xiong, G. Zeng, Z. Yang, Y. Zhou, C. Zhang and M. Cheng, *et al.*, Adsorption of tetracycline antibiotics from aqueous solutions on nanocomposite multi-walled carbon nanotube functionalized MIL-53(Fe) as new adsorbent, *Sci. Total Environ.*, 2018, **627**, 235–244.
10 P. Sethi, S. Barman and S. Basu, Strategic tuning of GO ratios in CuBTC-GO nanocomposites for next-generation tetracycline adsorption: A deep dive into isotherms, kinetics, and thermodynamics, *Sep. Purif. Technol.*, 2025, **361**, 131311.
11 S. Shao and X. Wu, Microbial degradation of tetracycline in the aquatic environment: a review, *Crit. Rev. Biotechnol.*, 2020, **40**(7), 1010–1018.
12 X. He, T. Kai and P. Ding, Heterojunction photocatalysts for degradation of the tetracycline antibiotic: a review, *Environ. Chem. Lett.*, 2021, **19**(6), 4563–4601.
13 H. Jiang, Q. Wang, P. Chen, H. Zheng, J. Shi and H. Shu, *et al.*, Photocatalytic degradation of tetracycline by using a regenerable (Bi)BiOBr/rGO composite, *J Cleaner Prod.*, 2022, **339**, 130771.
14 M. A. Abbasi, K. M. Amin, M. Ali, Z. Ali, M. Atif and W. Ensinger, *et al.*, Synergetic effect of adsorption-photocatalysis by GO−CeO_2 nanocomposites for photodegradation of doxorubicin, *J. Environ. Chem. Eng.*, 2022, **10**(1), 107078.
15 Z. Wu, Z. Chen, J. Chen, X. Ning, P. Chen and H. Jiang, *et al.*, Enhanced adsorption and synergistic photocatalytic degradation of tetracycline by MOF-801/GO composites via solvothermal synthesis, *Environ. Sci.: Nano*, 2022, **9**(12), 4609–4618.
16 M. Pourshaban-Mazandarani, M. Ahmadian, A. Nasiri and A. Poormohammadi, $CuCoFe_2O_4$@AC magnetic nanocomposite as a novel heterogeneous Fenton-like nanocatalyst for Ciprofloxacin degradation from aqueous solutions, *Appl. Water. Sci.*, 2023, **13**(9), 179.
17 A. Nasiri, M. R. Heidari, N. Javid and G. Yazdanpanah, New efficient and recyclable magnetic nanohybrid adsorbent for the metronidazole removal from simulated wastewater, *J. Mater. Sci.: Mater. Electron.*, 2022, **33**(33), 25103–25126.
18 A. Nasiri, M. Malakootian and N. Javid, Desalination and Water Treatment Modelling and optimization of lead adsorption by $CoFe_2O_4$@CMC@HZSM-5 from aqueous solution using response surface methodology, *Desalination Water Treat.*, 2022, **248**, 134–148.
19 G. Yazdanpanah, M. R. Heidari, N. Amirmahani and A. Nasiri, Heterogeneous Sono-Fenton like catalytic degradation of metronidazole by Fe_3O_4@HZSM-5 magnetite nanocomposite, *Heliyon*, 2023, **9**(6), e16461.
20 K. Althumayri, A. Guesmi, W. Abd El-Fattah, L. Khezami, T. Soltani, N. B. Hamadi and A. Shahat, Effective Adsorption and Removal of Doxorubicin from Aqueous Solutions Using Mesostructured Silica Nanospheres: Box–Behnken Design Optimization and Adsorption Performance Evaluation, *ACS Omega*, 2023, **8**(15), 14144–14159.
21 H. Furukawa, K. E. Cordova, M. O'Keeffe and O. M. Yaghi, The Chemistry and Applications of Metal-Organic Frameworks, *Science*, 2013, **341**(6149), 1230444.
22 M. X. Wu and Y. W. Yang, Metal–Organic Framework (MOF)-Based Drug/Cargo Delivery and Cancer Therapy, *Adv. Mater.*, 2017, **29**(23), 1606134.
23 T. Xia, Y. Lin, W. Li and M. Ju, Photocatalytic degradation of organic pollutants by MOFs based materials: A review, *Chin. Chem. Lett.*, 2021, **32**(10), 2975–2984.
24 T. Liu, Z. Li, X. Zhang, H. Tan, Z. Chen and J. Wu, *et al.*, Metal–Organic Framework-Intercalated Graphene Oxide Membranes for Selective Separation of Uranium, *Anal. Chem.*, 2021, **93**(48), 16175–16183.
25 J. Yu, C. Mu, B. Yan, X. Qin, C. Shen and H. Xue, *et al.*, Nanoparticle/MOF composites: preparations and applications, *Mater. Horiz.*, 2017, **4**(4), 557–569.
26 R. M. Rego, G. Sriram, K. V. Ajeya, H. Y. Jung, M. D. Kurkuri and M. Kigga, Cerium based UiO-66 MOF as a multipollutant adsorbent for universal water purification, *J. Hazard. Mater.*, 2021, **416**, 125941.
27 Y. Deng, L. Tang, G. Zeng, Z. Zhu, M. Yan and Y. Zhou, *et al.*, Insight into highly efficient simultaneous photocatalytic removal of Cr(VI) and 2,4-diclorophenol under visible light irradiation by phosphorus doped porous ultrathin g-C_3N_4 nanosheets from aqueous media: Performance and reaction mechanism, *Appl. Catal., B*, 2017, **203**, 343–354.
28 H. Yu, R. Shi, Y. Zhao, T. Bian, Y. Zhao and C. Zhou, *et al.*, Alkali-Assisted Synthesis of Nitrogen Deficient Graphitic Carbon Nitride with Tunable Band Structures for Efficient Visible-Light-Driven Hydrogen Evolution, *Adv. Mater.*, 2017, **29**(16), 1605148.
29 L. Zhang, X. Zhou, S. Liu, H. Liu, S. Zhu and Y. Mao, *et al.*, Two birds, one stone: Rational design of Bi-MOF/g-C_3N_4

photocatalyst for effective nitrogen fixation and pollutants degradation, *J. Cleaner Prod.*, 2023, **425**, 138912.

30 Y. Cao, L. Wang, C. Wang, X. Hu, Y. Liu and G. Wang, Sensitive detection of glyphosate based on a Cu-BTC MOF/g-C_3N_4 nanosheet photoelectrochemical sensor, *Electrochim. Acta*, 2019, **317**, 341–347.

31 A. H. Ragab, N. F. Gumaah, A. A. El Aziz Elfiky and M. F. Mubarak, Exploring the sustainable elimination of dye using cellulose nanofibrils- vinyl resin based nanofiltration membranes, *BMC Chem.*, 2024, **18**(1), 121.

32 Z. Durmus, R. Köferstein, T. Lindenberg, F. Lehmann, D. Hinderberger and A. W. Maijenburg, Preparation and characterization of Ce-MOF/g-C_3N_4 composites and evaluation of their photocatalytic performance, *Ceram. Int.*, 2023, **49**(14, Part B), 24428–24441.

33 D. Akgün and M. Dükkancı, g-C_3N_4 supported Ag/AgCl@MIL-88A MOF based triple composites for highly efficient diuron photodegradation under visible LED light irradiation, *J. Water Process Eng.*, 2023, **51**, 103469.

34 E. M. El-Fawal, S. A. Younis and T. Zaki, Designing $AgFeO_2$-graphene/$Cu_2(BTC)_3$ MOF heterojunction photocatalysts for enhanced treatment of pharmaceutical wastewater under sunlight, *J. Photochem. Photobiol., A*, 2020, **401**, 112746.

35 Y. Li, W. Qin, S. Chen, T. Gu, Y. Chen and F. Pei, *et al.*, Iron-based metal organic framework (Fe-MOF)-doped sesame stalk biochar enhances antibiotic degradation: Important role of free radicals and comparison of multiple degradation processes, *Sep. Purif. Technol.*, 2025, **353**, 128464.

36 A. A. E. A. Elfiky, M. F. Mubarak, M. Keshawy, I. E. T. El Sayed and T. A. Moghny, Novel nanofiltration membrane modified by metal oxide nanocomposite for dyes removal from wastewater, *Environ. Dev. Sustainability*, 2024, **26**(8), 19935–19957.

37 S. S. Y. Chui, S. M. F. Lo, J. P. H. Charmant, A. G. Orpen and I. D. Williams, A chemically functionalizable nanoporous material $[Cu_3(TMA)_2\ (H_2O)_3]_n$, *Science*, 1999, **283**(5405), 1148–1150.

38 S. Bordiga, L. Regli, F. Bonino, E. Groppo, C. Lamberti and B. Xiao, *et al.*, Adsorption properties of HKUST-1 toward hydrogen and other small molecules monitored by IR, *Phys. Chem. Chem. Phys.*, 2007, **9**(21), 2676–2685.

39 A. K. El-Sawaf, S. R. El-Dakkony, M. A. Zayed, A. M. Eldesoky, A. A. Nassar and A. El Shahawy, *et al.*, Green synthesis and characterization of magnetic gamma alumina nanoparticlesfor copper ions adsorption from synthetic wastewater, *Results Eng.*, 2024, **22**, 101971.

40 D. Monga, D. Ilager, N. P. Shetti, S. Basu and T. M. Aminabhavi, 2D/2d heterojunction of MoS2/g-C_3N_4 nanoflowers for enhanced visible-light-driven photocatalytic and electrochemical degradation of organic pollutants, *J. Environ. Manage.*, 2020, **274**, 111208.

41 H. J. Shin, K. K. Kim, A. Benayad, S. M. Yoon, H. K. Park and I. S. Jung, *et al.*, Efficient Reduction of Graphite Oxide by Sodium Borohydride and Its Effect on Electrical Conductance, *Adv. Funct. Mater.*, 2009, **19**(12), 1987–1992.

42 G. Zhang, C. Huang and X. Wang, Dispersing Molecular Cobalt in Graphitic Carbon Nitride Frameworks for Photocatalytic Water Oxidation, *Small*, 2015, **11**(9–10), 1215–1221.

43 S. Kumar, T. Surendar, A. Baruah and V. Shanker, Synthesis of a novel and stable g-C_3N_4–Ag3PO4 hybrid nanocomposite photocatalyst and study of the photocatalytic activity under visible light irradiation, *J. Mater. Chem. A*, 2013, **1**(17), 5333–5340.

44 V. Jabbari, J. M. Veleta, M. Zarei-Chaleshtori, J. Gardea-Torresdey and D. Villagrán, Green synthesis of magnetic MOF@GO and MOF@CNT hybrid nanocomposites with high adsorption capacity towards organic pollutants, *Chem. Eng. J.*, 2016, **304**, 774–783.

45 A. H. Ragab, B. S. Mettwally, M. F. Mubarak, A. Al-Ghamdi and M. Hemdan, Eco-friendly Electrospinning of Recycled Nylon 6,12 Waste for High-Performance Nonwoven Nanofibers in Sustainable Textile Applications, *J. Inorg. Organomet. Polym. Mater.*, 2024, **34**(4), 1491–1505.

46 Y. Chen, B. Zhai, Y. Liang, Y. Li and J. Li, Preparation of CdS/g-C_3N_4/MOF composite with enhanced visible-light photocatalytic activity for dye degradation, *J. Solid State Chem.*, 2019, **274**, 32–39.

47 Z. Huang, Q. Sun, K. Lv, Z. Zhang, M. Li and B. Li, Effect of contact interface between TiO_2 and g-C_3N_4 on the photoreactivity of g-C_3N_4/TiO_2 photocatalyst: (001) *vs.* (101) facets of TiO2, *Appl. Catal., B*, 2015, **164**, 420–427.

48 H. Niu, S. Liu, Y. Cai, F. Wu and X. Zhao, MOF derived porous carbon supported Cu/Cu_2O composite as high performance non-noble catalyst, *Microporous Mesoporous Mater.*, 2016, **219**, 48–53.

49 C. Zhao, Q. Yan, S. Wang, P. Dong and L. Zhang, Regenerable g-C_3N_4–chitosan beads with enhanced photocatalytic activity and stability, *RSC Adv.*, 2018, **8**(48), 27516–27524.

50 S. Singla, S. Basu and P. Devi, Solar light responsive 2D/2D $BiVO_4$/SnS_2 nanocomposite for photocatalytic elimination of recalcitrant antibiotics and photoelectrocatalytic water splitting with high performance, *J. Ind. Eng. Chem.*, 2023, **118**, 119–131.

51 L. Zhang, Y. Meng, H. Shen, J. Li, C. Yang and B. Xie, *et al.*, Photocatalytic degradation of rhodamine B by Bi_2O_3@LDHs S-scheme heterojunction: Performance, kinetics and mechanism, *Appl. Surf. Sci.*, 2021, **567**, 150760.

52 S. Singla, S. Sharma and S. Basu, MoS_2/WO_3 heterojunction with the intensified photocatalytic performance for decomposition of organic pollutants under the broad array of solar light, *J. Cleaner Prod.*, 2021, **324**, 129290.

53 B. Garg, P. Hait and S. Basu, Unlocking solar energy's potential: Dual photocatalytic activities of g-C_3N_4/Sb_2S_3 for hydrogen evolution and tetracycline degradation in sunlight, *J. Environ. Manage.*, 2024, **370**, 122403.

54 P. Wang and Q. Yuan, Photocatalytic degradation of tetracyclines in liquid digestate: Optimization, kinetics and correlation studies, *Chem. Eng. J.*, 2021, **410**, 128327.

55 G. Alnaggar, A. Hezam, Q. A. Drmosh and S. Ananda, Sunlight-driven activation of peroxymonosulfate by microwave synthesized ternary MoO_3/Bi_2O_3/g-C_3N_4 heterostructures for boosting tetracycline hydrochloride degradation, *Chemosphere*, 2021, **272**, 129807.

56 N. Mukwevho, R. Gusain, E. Fosso-Kankeu, N. Kumar, F. Waanders and S. S. Ray, Removal of naphthalene from simulated wastewater through adsorption-photodegradation by ZnO/Ag/GO nanocomposite, *J. Ind. Eng. Chem.*, 2020, **81**, 393–404.

57 N. Ghasemi, M. Ghasemi, S. Moazeni, P. Ghasemi, N. S. Alharbi and V. K. Gupta, *et al.*, Zn(II) removal by amino-functionalized magnetic nanoparticles: Kinetics, isotherm, and thermodynamic aspects of adsorption, *J. Ind. Eng. Chem.*, 2018, **62**, 302–310.

58 N. Wang, J. Chen, J. Wang, J. Feng and W. Yan, Removal of methylene blue by Polyaniline/TiO_2 hydrate: Adsorption kinetic, isotherm and mechanism studies, *Powder Technol.*, 2019, **347**, 93–102.

59 A. A. Inyinbor, F. A. Adekola and G. A. Olatunji, Kinetics, isotherms and thermodynamic modeling of liquid phase adsorption of Rhodamine B dye onto Raphia hookerie fruit epicarp, *Water Resour. Ind.*, 2016, **15**, 14–27.

60 M. F. Hussein, M. F. Mubarak, A. M. Al-Sirhani and R. Hosny, Examining the factors that impact the formation of barite scale in water injection operations: experimental study and quantification of scale formation, *Discover Appl. Sci.*, 2024, **6**(10), 519.

61 A. H. Ragab, N. F. Gumaah, A. A. El Aziz Elfiky and M. F. Mubarak, Exploring the sustainable elimination of dye using cellulose nanofibrils- vinyl resin based nanofiltration membranes, *BMC Chem.*, 2024, **18**(1), 121.

62 M. F. Mubarak, G. E. Khedr and H. M. El Sharkawy, Environmentally-friendly calcite scale mitigation: encapsulation of CDs@MS composite within membranes framework for nanofiltration, *J. Alloys Compd.*, 2024, **999**, 175061.

63 A. K. El-Sawaf, A. A. Nassar, A. A. El Aziz Elfiky and M. F. Mubarak, Advanced microcrystalline nanocellulose-based nanofiltration membranes for the efficient treatment of wastewater contaminated with cationic dyes, *Polym. Bull.*, 2024, **81**(14), 12451–12476.

64 N. Goyal, S. Barman and V. K. Bulasara, Efficient removal of bisphenol S from aqueous solution by synthesized nanozeolite secony mobil-5, *Microporous Mesoporous Mater.*, 2018, **259**, 184–194.

65 D. N. Mengesha, B. T. Shiferraw and H. Kim, Modification of the electronic structure of g-C_3N_4 using urea to enhance the visible light–assisted degradation of organic pollutants, *Environ. Sci. Pollut. Res.*, 2023, **30**(46), 102910–102926.

66 J. Zhang, C. Su, X. Xie and P. Liu, Huq MdE. Enhanced visible light photocatalytic degradation of dyes in aqueous solution activated by HKUST-1: performance and mechanism, *RSC Adv.*, 2020, **10**(61), 37028–37034.

67 A. Kundu, S. Sharma and S. Basu, Modulated BiOCl nanoplates with porous g-C_3N_4 nanosheets for photocatalytic degradation of color/colorless pollutants in natural sunlight, *J. Phys. Chem. Solids*, 2021, **154**, 110064.

68 C. Maggu, S. Singla and S. Basu, Unleashing the power of sunlight: Bi_2O_3/Sb_2S_3 photocatalysis for sustainable wastewater remediation of Tetracycline and Rhodamine-B, *J. Environ. Manage.*, 2024, **349**, 119424.

69 Y. Xiao, H. Wang, Y. Jiang, W. Zhang, J. Zhang and X. Wu, *et al.*, Hierarchical $Sb_2S_3/ZnIn_2S_4$ core–shell heterostructure for highly efficient photocatalytic hydrogen production and pollutant degradation, *J. Colloid Interface Sci.*, 2022, **623**, 109–123.

70 S. Singla, P. Devi and S. Basu, Highly Effectual Photocatalytic Remediation of Tetracycline under the Broad Spectrum of Sunlight by Novel $BiVO_4/Sb_2S_3$ Nanocomposite, *Catalysts*, 2023, **13**(4), 731.

71 H. Wang, M. Zhang, X. He, T. Du, Y. Wang and Y. Li, *et al.*, Facile prepared ball-like TiO_2 at GO composites for oxytetracycline removal under solar and visible lights, *Water Res.*, 2019, **160**, 197–205.